ELSEVIER

Volume 181, Number 5, May 2008

JOURNAL OF SOLID STATE CHEMISTRY

www.elsevier.com/locate/jssc

CONTENTS

Abstracted/indexed in BioEngineering Abstracts, Chemical Abstracts, Coal Abstracts, Current Contents/Physics, Chemical, & Earth Sciences, Engineering Index, Research Alert, SCISEARCH, Science Abstracts, and Science Citation Index. Also covered in the abstract and citation database SCOPUS®. Full text available on ScienceDirect®.

Regular Articles

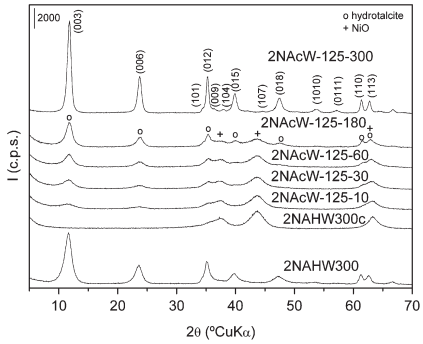

The microwave-assisted reconstruction of Ni,Al HTlcs with Ni/Al molar ratios 2/1 and 3/1 has been studied. Full recovering of the original layered structure is achieved in short periods of time for the 2/1 in the Na_2CO_3 solution, but more drastic conditions are necessary for the 3/1 samples and the reconstruction seems not to be completed. Only a partial reconstruction is observed in distilled water or NH_3 aqueous solution.

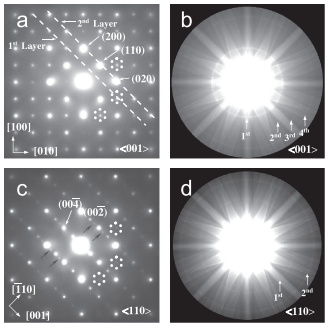

Selected area diffraction (SAD) and convergent beam electron diffraction (CBED) patterns taken along the (a,b) [001] and (c,d) [110] zones of the *Pbcm* phase from different domains. The occurrence of the FOLZ ring corresponding to 15.5 Å and the superlattice spots as indicated by black arrows confirming the existence of the cell-doubled antiferroelectric phase. Coexistence of the *Pbnm* and *Pbcm* phases across the transition, i.e. at room temperature, has been observed and attributed to the strain/disorder-induced broadening of the first-order antiferroelectric phase transition.

Regular Articles—Continued

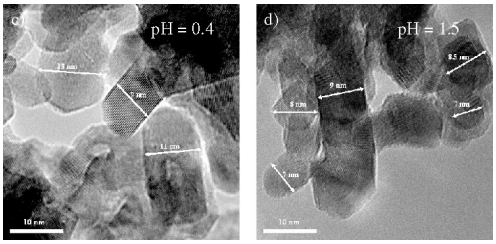

Nanosized crystals of RuO_2 prepared by sol gel route, at pH = 0.4 and 1.5. Mean size values $\langle D \rangle$, respectively, 10 and 8 nm.

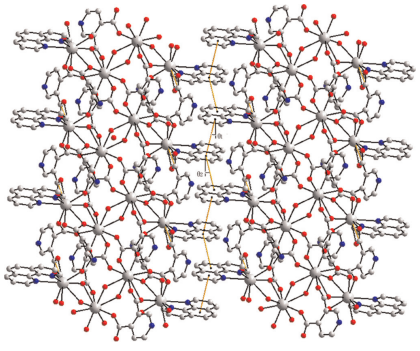

Two novel lanthanide coordination polymers $[M_2(pydc)_3(phen)(H_2O)\cdot H_2O]_n$ (M = Eu(**1**) and Tb(**2**), pydc = pyridine-3,4-dicarboxylate, phen = 1,10-phenthroline) have been synthesized and characterized. Both compounds reveal a one-dimensional nano-chain, which is further assembled into a three-dimensional supramolecular network via π–π stacking interactions and hydrogen bonds. Their luminescent and magnetic properties have been investigated.

The excited state dynamics of $KLa(MoO_4)_2$:Pr^{3+}: From a case study to the determination of the energy levels of rare earth impurities relative to the bandgap in oxidising host lattices
Enrico Cavalli, Philippe Boutinaud, Marco Bettinelli and Pieter Dorenbos
page 1025

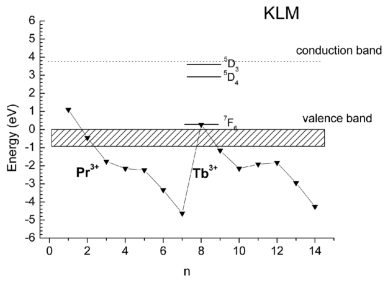

The study of the excited state dynamics of $KLa(MoO_4)_2$ single crystals doped with Pr^{3+} allows to determine the energies of the levels of the active ion relative to the valence and conduction bands of the host. This model has then been extended to the other rare earth ions on the basis of the systematic nature of the lanthanide energy levels properties.

Hybrid materials of MCM-41 functionalized by lanthanide (Tb^{3+}, Eu^{3+}) complexes of modified *meta*-methylbenzoic acid: Covalently bonded assembly and photoluminescence
Ying Li and Bing Yan
page 1032

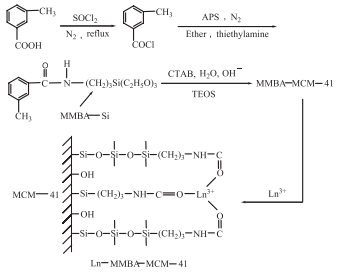

Novel organic–inorganic mesoporous luminescent materials were synthesized by linking lanthanide (Tb^{3+}, Eu^{3+}) complexes to covalently bond the functionalized ordered mesoporous MCM-41 with modified *meta*-methylbenzoic acid (MMBA)-Si by co-condensation of tetraethoxysilane (TEOS) in the presence of the cetyltrimethylammonium bromide (CTAB) surfactant as template.

Correlation between structural features and vis–NIR spectra of α-Fe_2O_3 hematite and AFe_2O_4 spinel oxides (A = Mg, Zn)
N. Pailhé, A. Wattiaux, M. Gaudon and A. Demourgues
page 1040

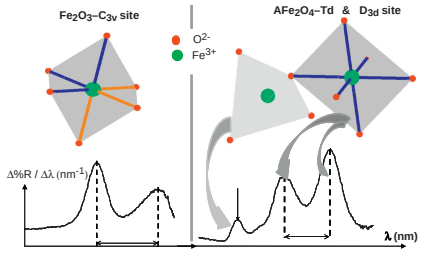

UV–visible–NIR reflectance of iron red pigments: $MgFe_2O_4$, $ZnFe_2O_4$ spinels and Fe_2O_3 hematite, were analyzed in regard of their structural features: cationic distribution, geometry of the Fe^{3+} sites, iono-covalence of the bonds.

Cooperative self-construction and enhanced optical absorption of nanoplates-assembled hierarchical Bi_2WO_6 flowers
Shengwei Liu and Jiaguo Yu
page 1048

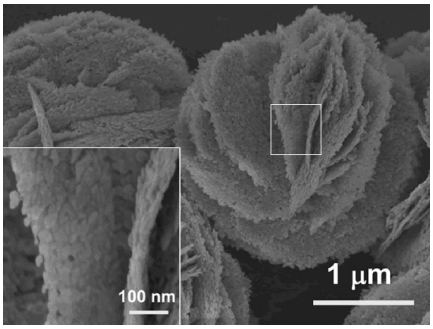

Bi_2WO_6 hierarchical multilayered flower-like assemblies are fabricated on a large scale by a simple hydrothermal method in the presence of polymeric poly(sodium 4-styrenesulfonate).

Synthesis, structure and electric studies for $La_{0.7}A_{0.3}Mn_{0.96}(In_xAl_{(1-x)})_{0.04}O_3$; A = Ca and Sr perovskites
M.F. Mostafa, S.S. Ata-Allah and H.S. Refai
page 1056

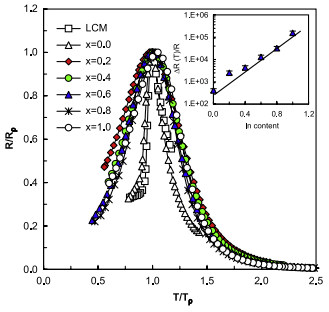

The reduced resistivity $[R(T)/R(T_\rho)]$ vs. the reduced temperature $[T/T_\rho]$ of (Al and In) doped $La_{0.7}Ca_{0.3}MnO_3$-manganites. The variation of the amplitude of the giant resistive peak $\Delta R(T)/R = [R(T_\rho) - R(T_{288}K)]/R(T_{288}K)$ with In content x (inset).

The phase diagram GdF_3–LuF_3
I.M. Ranieri, S.L. Baldochi and D. Klimm
page 1070

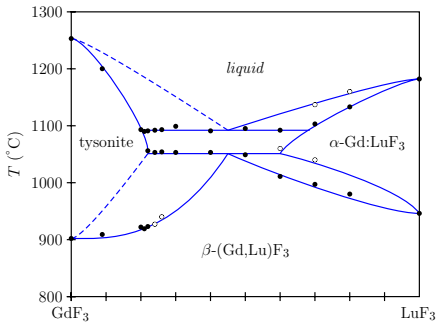

The phase diagram GdF_3-LuF_3, α, β mean high-T phase or low-T phase, respectively.

Continued

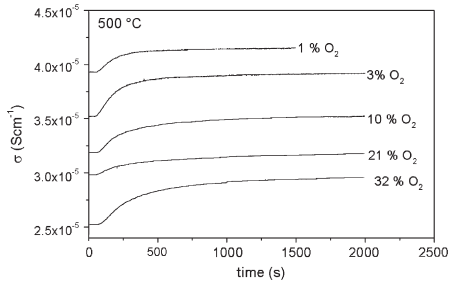

Temporal dependence of electrical conductivity at 500 °C for γ'-Bi_2MoO_6 at controlled partial pressures of oxygen.

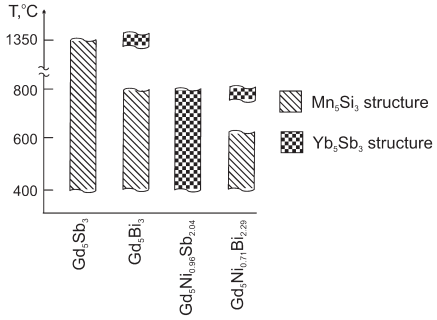

Ni substitution of Sb in Gd_5Sb_3 and Gd_5Bi_3 leads to the formation of the orthorhombic Yb_5Sb_3-type structure for $Gd_5Ni_{0.96}Sb_{2.04}$ and stabilizes the orthorhombic bismuthide $Gd_5Ni_{0.71}Bi_{2.29}$ to lower temperatures. Magnetic behavior and magnetocaloric effect was studied for hexagonal Mn_5Si_3-type Gd_5Bi_3, and orthorhombic $Gd_5Ni_{0.96}Sb_{2.04}$ and $Gd_5Ni_{0.71}Bi_{2.29}$.

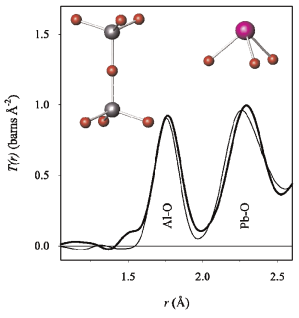

Combined neutron powder diffraction and total scattering, and ^{27}Al NMR on crystalline $Pb_9Al_8O_{21}$ shows it to be a non-stoichiometric compound with vacancies due to PbO volatilisation. A detailed consideration of the thermal and static disorder is given, showing that glass and crystal phases have very similar disorder at short range.

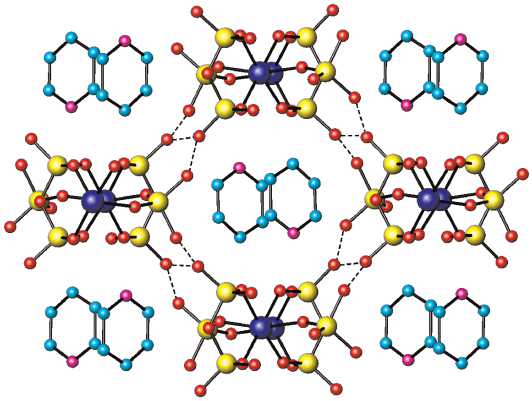

The low temperature hydrothermal synthesis offers many possibilities in the preparation of new materials with mixed octahedral–tetrahedral open-frameworks. $Fe(H_2PO_4)(H_2P_2O_7)\cdot C_5H_5N$ is constituted by linear chains of FeO_6 octahedra joined through of both dihydrogenphosphate and dihydrogendiphosphate bridges, interconnected by hydrogen bonds, originating channels where the pyridine molecules are located.

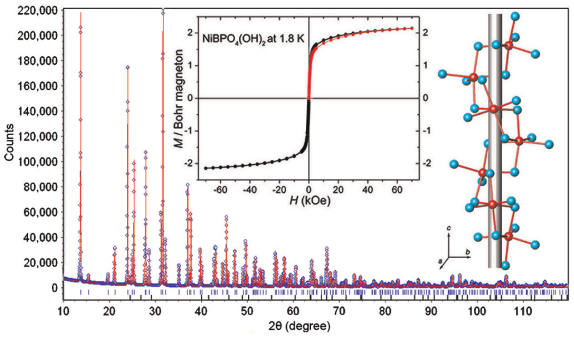

Two isotypic borophosphates $MBPO_4(OH)_2$ (M = Mg, Ni) have been hydrothermally synthesized and structurally characterized by powder X-ray diffraction in the space group $P3_121$. Nickel (or magnesium) atoms are octahedrally coordinated, which further share edges forming NiO_6 chains around the three-fold screw-axis. Magnetic investigation of $NiBPO_4(OH)_2$ shows that it is a quasi-one-dimensional magnet, where the intra- and inter-chain interactions are proved to be both ferromagnetic, and a long-range ordering is established below 2.2 K.

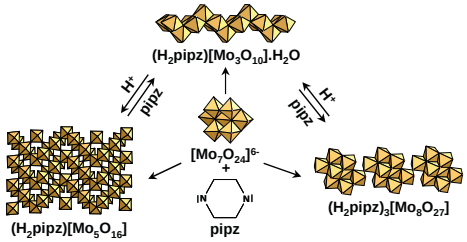

Three organic–inorganic hybrid materials have been prepared from the investigations of the $[Mo_7O_{24}]^{6-}$/piperazine system in hydrothermal conditions. The role of the pH on the stabilization of the different polyoxomolybdate blocks in the materials i.e. $^{1}_{\infty}[Mo_3O_{10}]^{2-}$ and $^{1}_{\infty}[Mo_8O_{27}]^{6-}$ chains and $^{2}_{\infty}[Mo_5O_{16}]^{2-}$ layer has been investigated.

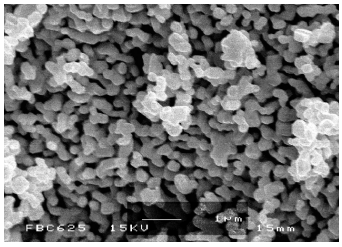

Scanning electron micrograph of $La_4Ni_3O_{10}$ (bar = 1 μm) made by a single heat treatment at 1075 °C in air for 12 h of a 4:3 La:Ni ratio co-crystallite mixture of the metal hydroxides.

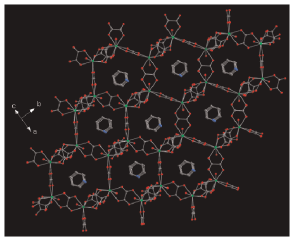

Two novel 3-D extended porous coordination polymers have been synthesized by hydrothermal method. Both compounds are 3-D open-framework structures with a 6^6 uniform net, which consist of honeycomb-like layers connected to each other by oxalate units. While different guest molecules fill in their cavities of honeycomb-like layers. Study of ultrasonic treatment on **2** indicates the replacement of NH_4^+ by K^+ on potassium ion exchange.

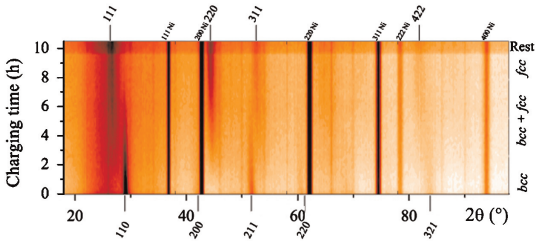

2D projection of the neutron diffraction pattern intensities as function of time during electrochemical charge of Pd-doped $Mg_{0.65}Sc_{0.35}$ active material showing the progressive transformation from bcc to fcc.

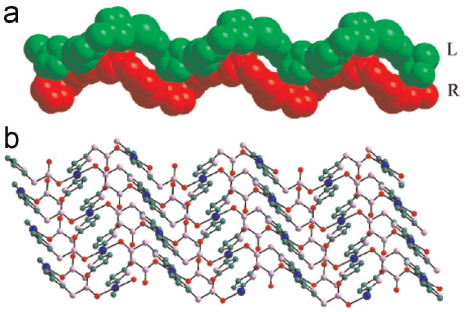

Two novel coordination polymers, $[Ag(tza)]_{\infty}$ (**1**) and $[Cu(tza)_2]_{\infty}$ (**2**) have been prepared and characterized. Compound **1** features extended double-stranded helical chains. Compound **2** features undulated layered structure with hourglass-shaped $[Cu_4(tza)_4]$ as subunits with the weak ferromagnetic interactions between Cu(II) ions.

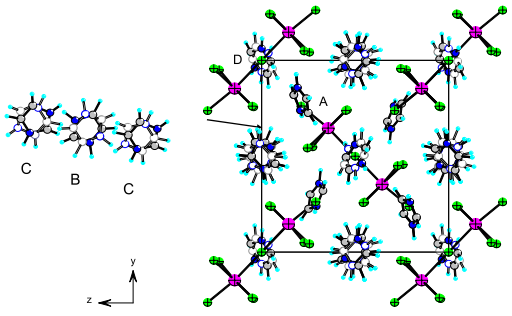

Crystal packing down the *a*-axis in $(C_3N_2H_5)_5Sb_2Br_{11}$ in plane **II** at 155 K.

Continued

$IrSr_2TbCu_2O_8$, a high-pressure metamagnetic cuprate: Structure, microstructure and properties

A.J. Dos santos-García, J. van Duijn, R. Saéz-Puche, G. Heymann, H. Huppertz and M.Á. Alario-Franco

page 1167

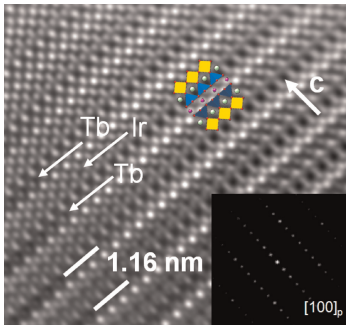

Reconstructed image from the SAED of the long *c* tetragonal axis ($3a_p$) of a $IrSr_2TbCu_2O_8$ crystal. A unit cell picture is included for comparison.

Spatially selected synthesis of LaF_3 and Er^{3+}-doped CaF_2 crystals in oxyfluoride glasses by laser-induced crystallization

M. Kusatsugu, M. Kanno, T. Honma and T. Komatsu

page 1176

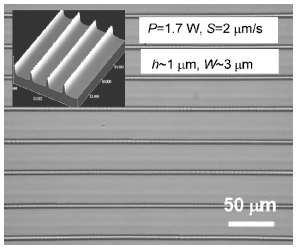

This figure shows the polarization optical and confocal scanning laser micrographs for lines obtained by laser irradiations with a laser power of $P = 1.7$ W and a scanning speed of $S = 2$ μm/s in an oxyfluoride glass. It is proposed that the line consists of the composite of CaF_2 nanocrystals and oxide glassy phase. This is the first demonstration on the patterning of fluoride crystals in glass by laser irradiations.

Hybrid structures formed by homo- and heteroleptic aliphatic dicarboxylates of lead with 2-D inorganic connectivity

A. Thirumurugan and C.N.R. Rao

page 1184

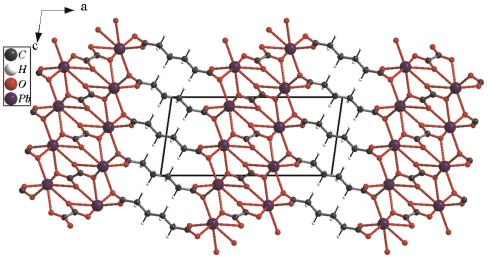

Three homoleptic and two heteroleptic three-dimensional lead aliphatic dicarboxylates along with a novel two-dimensional lead nitrate-oxalate with hybrid structures involving Pb–O–Pb linkages have been synthesized and charecterized. In all these dicarboxylates, there is two-dimensional inorganic connectivity. The lead (II) cation has hemi- or holo-directed coordination geometry.

Multivariate data analysis approach to understand magnetic properties of perovskite manganese oxides

N. Imamura, T. Mizoguchi, H. Yamauchi and M. Karppinen

page 1195

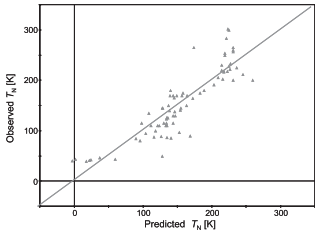

Statistical multivariate data analysis techniques are applied to detect structure-property relations in antiferromagnetic (AFM) and ferromagnetic (FM) manganese perovskites. For AFM compounds, *partial least squares projections to latent structures* analysis predict the magnitude of the Néel temperature on the bases of structural parameters only. Moreover, AFM and FM compounds are well separated by means of so-called *partial least squares discriminant analysis* method.

Powder preparation and UV absorption properties of selected compositions in the CeO_2–Y_2O_3 system

Franck Tessier, François Cheviré, Francisco Muñoz, Odile Merdrignac-Conanec, Roger Marchand, Michel Bouchard and Christophe Colbeau-Justin

page 1204

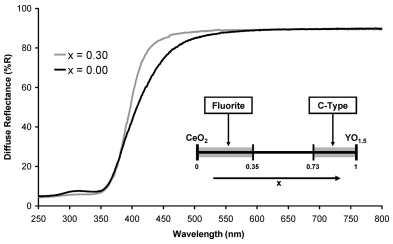

Comparison between diffuse reflectance spectra of ceria ($x = 0$) and yttrium modified ceria ($x = 0.3$).

Synthesis and characterization of a new layered organic–inorganic hybrid nickel(II) 1,4:5,8-naphthalenediimide *bis*-phosphonate, exhibiting canted antiferromagnetism, with T_c~21 K

Elvira M. Bauer, Carlo Bellitto, Carlos J. Gómez García and Guido Righini

page 1213

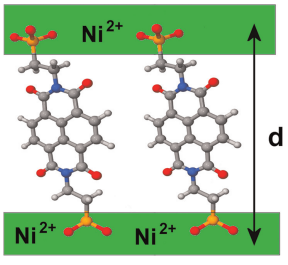

A new layered hybrid organic–inorganic Ni(II) *N*,*N*′-*bis*(2-phosphonoethyl)-naphthalene 1,4:5,8 tetracarboxydiimide complex has been synthesized and characterized. Magnetic measurements as a function of temperature and at different fields show that the compound is magnetically ordered below T_c~21 K.

Impact of metal substitutions for cobalt in $YBaCo_4O_7$
A. Maignan, V. Caignaert, V. Pralong, D. Pelloquin and S. Hébert
page 1220

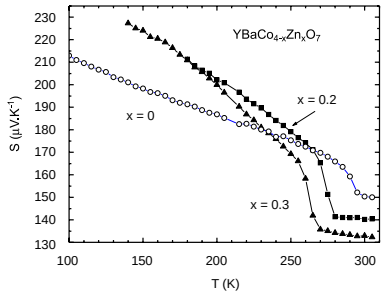

The temperature characteristic of the structural transition in $YBaCo_4O_7$, indicated by an abrupt jump of the Seebeck coefficient, decreases as Zn^{2+} is substituted for cobalt. In contrast, Al^{3+} or Ga^{3+} substitutions suppress this structural transition.

Effect of heat treatment on pore structure in nano-crystalline NiO: A small angle neutron scattering study
J. Bahadur, D. Sen, S. Mazumder and S. Ramanathan
page 1227

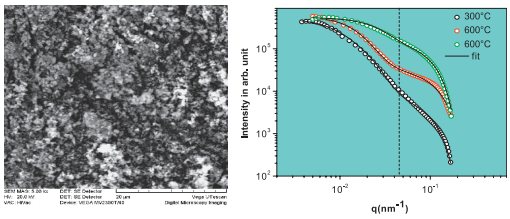

SEM micrograph shows the microstructure of the nano-crystalline NiO. An average agglomerate size of ~1 μm is evident from SEM and LS.SANS profiles for the samples heat treated at 300, 600 and 900 °C, respectively, are shown. A significant variation in the profile shape due to the modification in the intra-agglomerate pore structure under heat treatment is visible.

Chiolite-like $Ca_5Te_3O_{14}$: An X-ray and neutron diffraction study
W.T. Fu and D.J.W. IJdo
page 1236

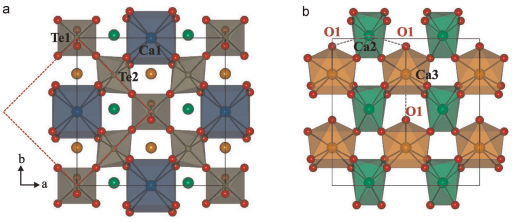

The structure of $Ca_5Te_3O_{14}$ around $z = 0$(a) and 0.25(b), respectively. The dimension of the unit cell is drawn in full line and that of the sub-cell in dashed line. In (b) the relatively too long Ca2–O1 and Ca3–O1 bond distances are also shown in dashed line.

Pressure induced phase transformation in $U_2O(PO_4)_2$
A.K. Mishra, Chitra Murli, A. Singhal and Surinder M. Sharma
page 1240

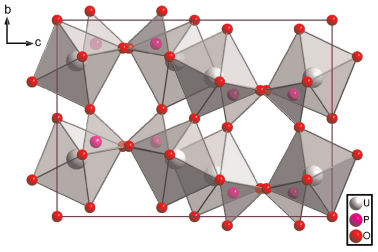

The high pressure behavior of $U_2O(PO_4)_2$ has been investigated with the help of Raman scattering and X-ray diffraction measurements up to ~14 and 6.5 GPa, respectively. The observed changes in the Raman spectra as well as the X-ray diffraction patterns suggest that $U_2O(PO_4)_2$ undergoes a phase transition at ~6 GPa to a mixture of a disordered ambient pressure phase and a new high pressure phase. The new phase resembles the triclinic mixed-valence phase of uranium orthophosphate ($U(UO_2)(PO_4)_2$). On release of pressure the initial phase is not retrieved.

Shape controlled synthesis of $CaMoO_4$ thin films and their photoluminescence property
Ana Paula de Azevedo Marques, Valeria M. Longo, Dulce M.A. de Melo, Paulo S. Pizani, Edson R. Leite, José Arana Varela and Elson Longo
page 1249

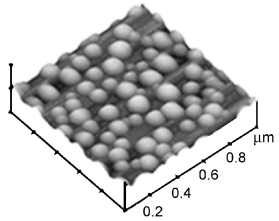

$CaMoO_4$ thin films were prepared by the complex polymerization method (CPM). The films were annealed at different temperatures and time in a conventional resistive furnace and in a microwave oven. A strong photoluminescence emission was observed in the disordered thin films and was attributed to complex cluster vacancies. The experimental results were confirmed by high level first principle calculations.

Crystal chemistry of the divalent cation in alluaudite-type phosphates: A structural and infrared spectral study of the $Na_{1.5}(Mn_{1-x}M_x^{2+})_{1.5}Fe_{1.5}(PO_4)_3$ solid solutions ($x = 0$ to 1, $M^{2+} = Cd^{2+}$, Zn^{2+})
Frédéric Hatert
page 1258

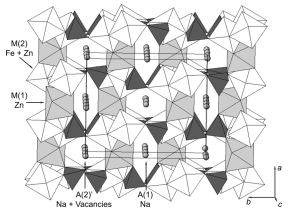

The crystal structure of $Na_{1.5}Zn_{1.5}Fe_{1.5}^{3+}(PO_4)_3$.

Continued

Rapid Communications

High pressure synthesis and structure of a new magnetoplumbite-type cobalt oxide $SrCo_{12}O_{19}$
Shintaro Ishiwata, Ichiro Terasaki, Masaki Azuma and Mikio Takano
page 1273

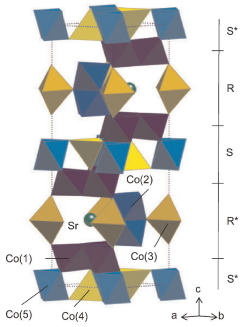

A new magnetoplumbite-type hexagonal cobalt oxide, $SrCo_{12}O_{19}$, has been synthesized by a high-pressure technique. Bond-valence calculations based on a single crystal X-ray structure refinement show a rather wide charge distribution for Co sites from +2.15 (Co(4)) to +3.50 (Co(1)).